Catalysis Science & Technology

ROYAL SOCIETY OF CHEMISTRY

COMMUNICATION

View Article Online
View Journal | View Issue

Open Access Article. Published on 13 February 2024. Downloaded on 12/5/2025 3:20:50 AM.
This article is licensed under a Creative Commons Attribution-NonCommercial 3.0 Unported Licence.

Check for updates

Cite this: *Catal. Sci. Technol.*, 2024, **14**, 1480

Received 8th January 2024,
Accepted 13th February 2024

DOI: 10.1039/d4cy00031e

rsc.li/catalysis

Probing current density distribution over a catalyst layer at the micrometer scale in a water electrolyzer†

Yaping Pan,‡[ab] Han Liu,‡[ab] Jiawei Liu,[ab] Linrui Wen,[b] Kejie Lao,[ab] Shuirong Li,[d] Xiaoliang Fang,[d] Huakun Wang,*[c] Hua Bing Tao*[ab] and Nanfeng Zheng[ab]

A better understanding of current density distribution, *i.e.* the true electrochemical reaction behavior, in electrochemical energy devices has long been desired. However, it is considered very challenging to comprehensively observe the current density within real PEMWE devices at the micrometer scale as the components are densely assembled by metal plates. Thus, an *ex situ* method for micron-level current density detection is proposed in this study, where the highly active but unstable characteristic of RuO_2 in the oxygen evolution reaction (OER) in acidic media was fully utilized. Compared to the average current density at the macrometer scale, the detection of current density at the micrometer scale can provide more valuable insights for the rational design of low iridium loading membrane electrodes. Our study showed that the border area of the PTL/CL interface exhibited the highest current density under any working condition. The untouched area exhibited the lowest current density because of poor conditions, which can be attributed to the combined effects of conductivity and mass transfer. Besides, an experimentally validated numerical model was also proposed, and the simulation results indicated that porosity was the most critical factor affecting the performance of PEMWE, and the optimized porosity was about 0.3. The new insights into the localized current density derived from this method open a new avenue for optimization of the performance and cost reduction of PEMWE.

The replacement of traditional fossil fuels with renewable energy sources is inevitable for reducing carbon emissions. Hydrogen, an environmentally friendly energy carrier, plays a key role in achieving sustainable development.[1–5] Among the various technologies for hydrogen production, water electrolysis, especially proton exchange membrane water electrolysis (PEMWE), has attracted significant attention owing to its compactness, mild operating conditions, and environmental cleanliness.[6–8] However, due to the intricate internal reaction mechanism of PEMWE, characterized by its multidomain and multiscale coupling features, different local conditions in PEMWE can lead to the non-uniform distribution of species, heat, and Ir-based catalyst utilization, resulting in uneven current density distribution. The ramifications of this nonuniformity are becoming increasingly pronounced in commercial-scale applications.[9–11]

Unfortunately, in practical PEMWE devices, the tight assembly of their components using dense metal plates makes it challenging to accurately observe and probe internal information. Several detection methods have been reported to directly study the current density distribution of PEMWE and PEMFCs. Approximately 100 literature reports on the methods for analyzing the current density distribution of PEM cells were surveyed in this study; however, only 24.3% of those have focused on techniques for investigating the current density distribution of PEMWE, which included electrochemistry, printed circuit boards (PCBs),[12–14] sensing wires,[15,16] and high-speed and microscale visualization systems (HMVSs),[17–20] as illustrated in Fig. 1(a). However, each of these methods has certain limitations. For instance, methods based on electrochemistry are restricted to analyzing current density distribution on a macro-electrolytic cell scale. Moreover, while the resolution of PCBs and sensing wires is higher compared with electrochemistry, their device assembly is difficult and does not reflect or give true information on real working conditions. The utilization of HMVSs allows for the identification of current density distribution by observing the information of bubbles, and it

[a] State Key Laboratory for Physical Chemistry of Solid Surfaces, Collaborative Innovation Center of Chemistry for Energy Materials, and College of Chemistry and Chemical Engineering, Xiamen University, Xiamen 361005, China. E-mail: hbtao@xmu.edu.cn
[b] Innovation Laboratory for Sciences and Technologies of Energy Materials of Fujian Province (IKKEM), Xiamen 361005, China
[c] Fujian Key Laboratory of Digital Simulations for Coastal Civil Engineering, Xiamen University, Xiamen 361005, China. E-mail: hkwang@xmu.edu.cn
[d] College of Energy, Xiamen University, Xiamen 361005, China

† Electronic supplementary information (ESI) available. See DOI: https://doi.org/10.1039/d4cy00031e

‡ These authors contributed equally to this work.

This journal is © The Royal Society of Chemistry 2024

Open Access Article. Published on 13 February 2024. Downloaded on 12/5/2025 3:20:50 AM.
This article is licensed under a Creative Commons Attribution-NonCommercial 3.0 Unported Licence.

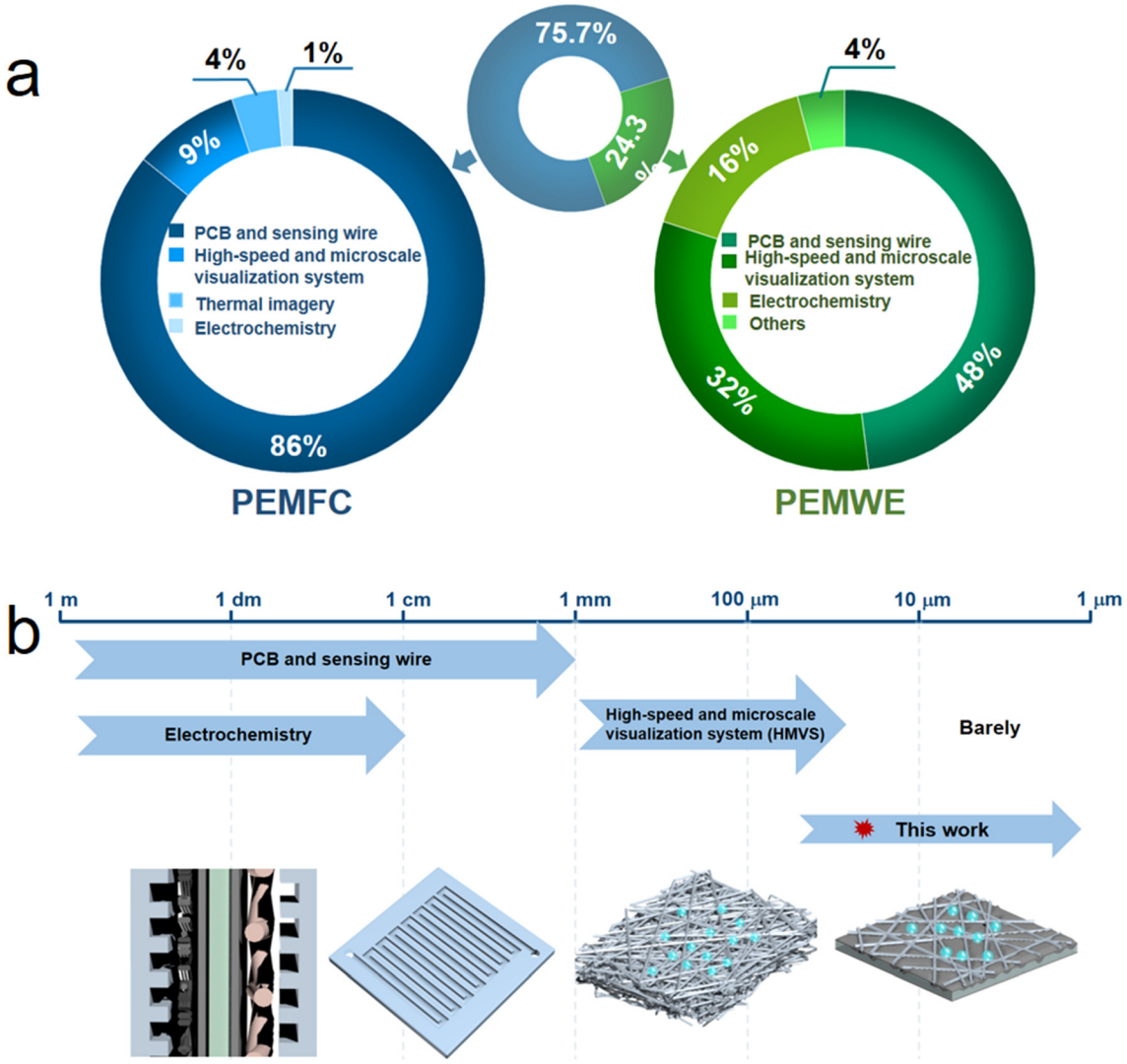

Fig. 1 (a) Proportions of publications that are focused on the current density distribution in PEM water electrolysis (PEMWE) and PEM fuel cells (PEMFCs) based on approximately 100 publications in total. (b) Field of view of the diverse research techniques applicable to the study of the current density distribution of PEMWE.

has revealed that the primary origin of current density can be traced back to the interface between a porous transport layer (PTL) and catalyst layer (CL). While these methods offer information on the micron-scale current density distribution, their qualitative analysis is generally insufficient for a comprehensive and profound understanding of the current density distribution under working conditions, especially in the contact area between the PTL and CL. This limitation hinders the loading reduction and efficient utilization of Ir-based catalysts, as shown in Fig. 1(b). Hence, there is a crucial need to develop novel approaches for assessing smaller scales of current density distribution under actual operating conditions.

RuO_2 has garnered considerable interest as a catalyst for the OER in acidic conditions owing to its exceptional activity. However, its inherent instability poses a significant drawback, given that Ru species tend to separate as volatile high-valence oxides during the OER process,[21–26] as confirmed by RRDE[27] and eQCM[28] tests, as shown in Fig. S1.† To study the stability of RuO_2 under real working conditions, we conducted tests with a single PEMWE cell with RuO_2 as the anode catalyst. Aging tests of RuO_2 as the anode catalyst were carried out at 1.8 V, as shown in Fig. S2,† and we accidentally discovered that the electrochemical performance of the aged single cell could be partially recovered when the Ti mesh was rotated 90 degrees, as shown in Fig. 2(a and b). This phenomenon suggested the non-uniform distribution of current density over the CL surface. At the same time, EIS diagnostics were used to obtain R_{ct} and R_{ohm}, where the former represents the charge transfer for electrochemical reactions of the OER and the latter represents the proton and electron transport resistance. A 20 mV perturbation amplitude was used to ensure high-quality results. After the aging test, the amorphization of the catalyst or the dissolution of high-valent compounds led to a sharp increase in both R_{ct} and R_{ohm}. Simultaneously,

Open Access Article. Published on 13 February 2024. Downloaded on 12/5/2025 3:20:50 AM.
This article is licensed under a Creative Commons Attribution-NonCommercial 3.0 Unported Licence.

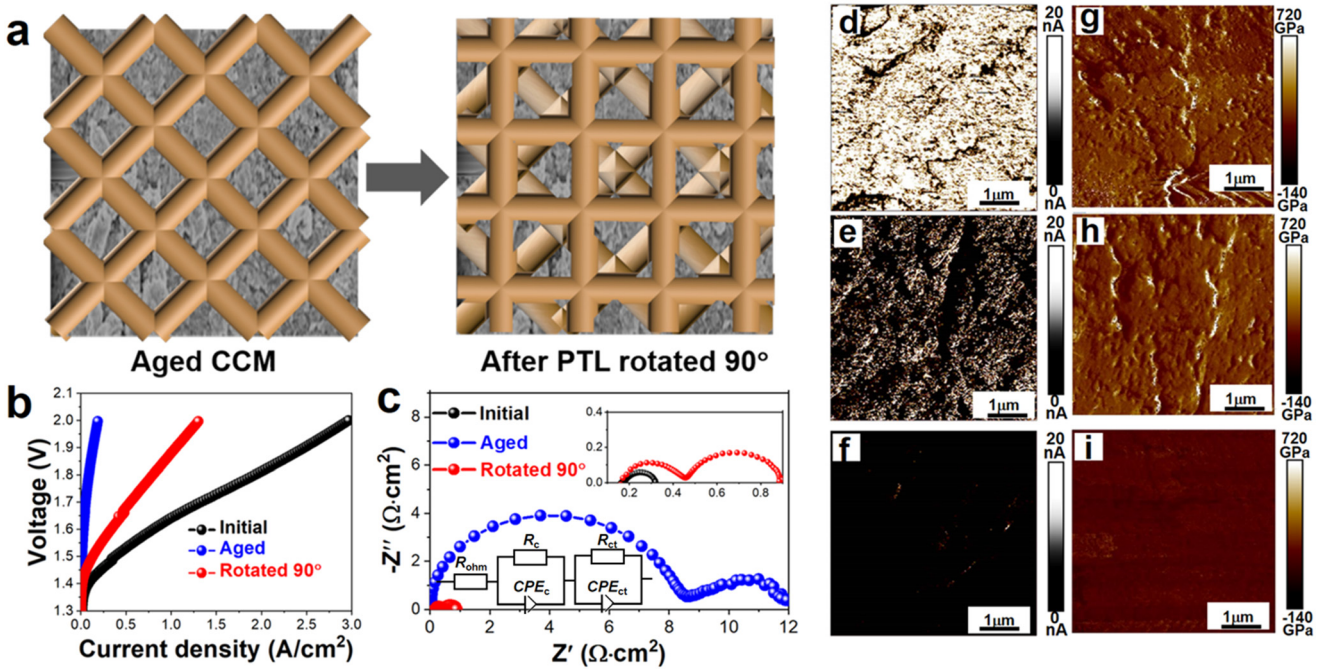

Fig. 2 (a) Schematic diagram of the Ti mesh rotated 90 degrees before and after the aging test. (b) Polarization curve of the RuO_2 catalyst before and after the aging test at 1.8 V. (c) Impedance spectra before and after the aging test at 1.8 V. AFM measured for CL before (d and g) and after aging in zone (1) (e and h) and zone (2) (f and i). (d, e, and f) Conductivity of CL by the AFM test. (g, h, and i) stiffness of CL by the AFM test.

significant interface resistance occurred in the high-frequency region, denoted as R_c, impeding electron transmission and diminishing the electrochemical performance of PEMWE, as illustrated in Fig. 2(b), S3, and Fig. S4.†[29] When the Ti mesh was rotated 90 degrees, R_{ct}, R_{ohm} and R_c were moderately reduced, consistent with the polarization curve trend.

Fig. S5† shows the morphology of the fresh and aged CL as measured by scanning electron microscopy (SEM), as shown in Fig. S5(a).† Clear differences could be observed between the two samples, with the aged CL exhibiting regular indentations from the Ti mesh. To distinguish between the surface areas of the CL, the region pressed by the Ti fiber was labeled as "(2)," while the remaining area was denoted as "(1)". Atomic force microscopy (AFM) was employed to further investigate the differences in the CL composition. AFM images of the fresh and aged CL were obtained at various locations and analyzed for assessing the topography, current mapping, and stiffness. In the topography images, the fresh and aged CL at different locations had a similar roughness, as shown in Fig. S5(b).† The electronic current at the CL was influenced by the content of RuO_2 and the ionomer, with a higher RuO_2 content leading to a higher electronic current. At a bias voltage of 1 V, the electronic current on the CL was detected and appeared grainy, reflecting the multi-component composition of the CL, including RuO_2 and the ionomer, as shown in Fig. 2(d–f).[30,31] The area of (1) had the second highest conductivity, while the area of (2) had the lowest conductivity, indicating that the content of RuO_2 followed the opposite order. Stiffness mapping revealed that region (2) was stiffer than region (1), as shown in Fig. 2(g–i). The AFM data further revealed the non-uniform distribution of the current density on the surface of the CL.

In this work, we developed an *ex situ* visualization method to study the current density distribution at the micrometer scale by exploiting the unstable property of RuO_2 under acidic OER conditions, as shown in Fig. 3(e). Scanning electron microscopy (SEM) and energy dispersive X-ray spectroscopy (EDS) were employed to evaluate the Ru element content at various locations on the CL. The region with a lower content of the Ru element exhibited a higher distribution of current density, attributable to a faster electrochemical reaction and a greater precipitation of the Ru element. Since IrO_2 is a stable OER catalyst, the Ir element was utilized as the calibration element to determine the Ru element content on the CL surface.[32,33] As shown in Fig. S6,† aging tests of IrO_2 + RuO_2 as the anode catalyst were performed at 1.5, 1.8, and 2.1 V, respectively, until the current density reached 0.1 mA cm^{-2}. Obviously, the cell voltage at 1.5 V took the longest time, lasting 16 h. Also, the endurance time was 2 h at 1.8 V and 2.1 V. The content of Ru element was determined at seven symmetrical positions at the interface between the Ti fiber and the aged CL using SEM and EDS, as illustrated in Fig. 3(d) and S9.† In order to better analyze the experimental results, the PTL/CL interface was classified into three distinct regions: the untouched area, border area, and touched area. Among these, the untouched area consisted of site1 and site7, the border area comprised site2 and site6, while the touched area encompassed site3, site4 and site5, as shown in Fig. 3(e).

Open Access Article. Published on 13 February 2024. Downloaded on 12/5/2025 3:20:50 AM.
This article is licensed under a Creative Commons Attribution-NonCommercial 3.0 Unported Licence.

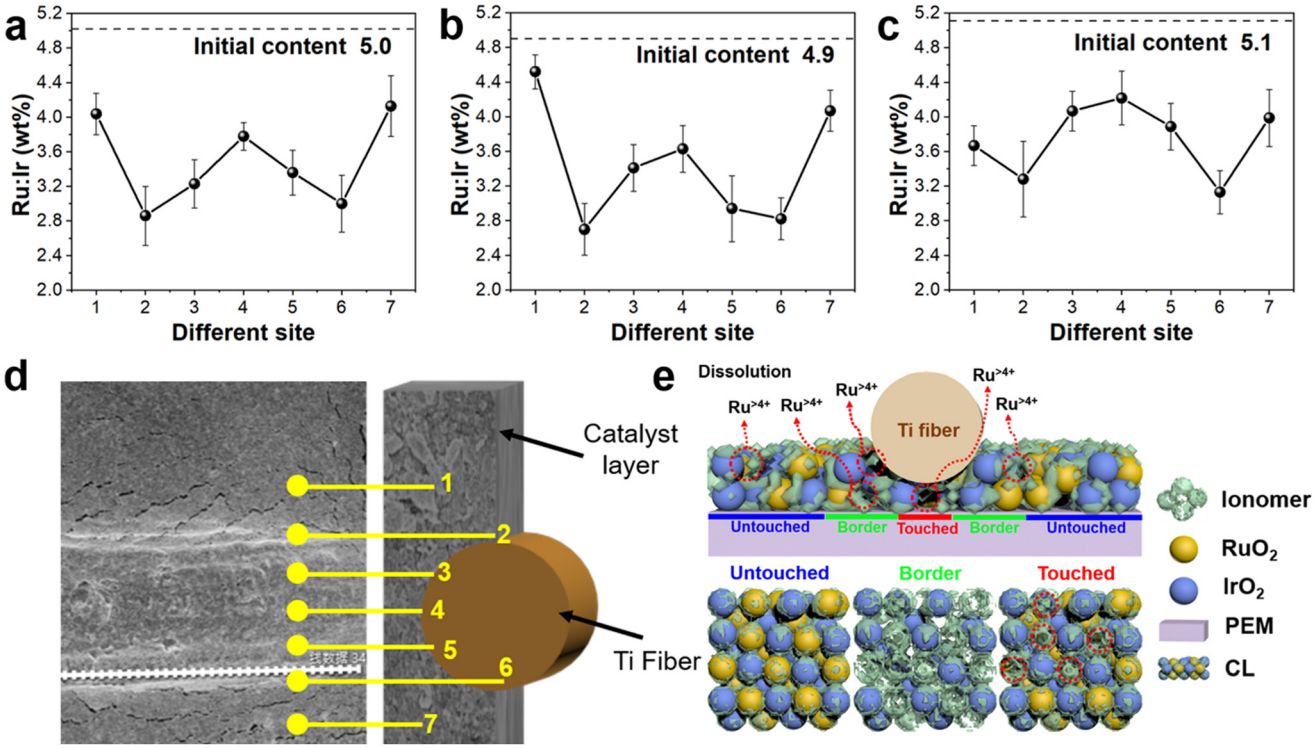

Fig. 3 Content of Ru element at 7 symmetrical positions after the aging tests at (a) 1.5 V, (b) 1.8 V, and (c) 2.1 V. (d) Schematic of the interfacial contact between the CL and Ti fiber after the aging test; 7 of the symmetrical positions are highlighted with yellow lines, where 1 and 7, 2 and 6, 3 and 5 are symmetrical sites. (e) Schematic diagram of the method for studying the current density distribution at the micrometer scale by exploiting the unstable property of RuO_2 under acidic OER conditions, in which the Ir element was utilized as the calibration element to determine the Ru element content on the CL surface.

The Ru element content on the CL surface was analyzed in the aging test at 1.5 and 1.8 V as depicted in Fig. 3(a and b). Site2 and site6 exhibited the lowest Ru element content and highest current density distribution for the CL, which were located at the border area of the PTL/CL interface, fully meeting the requirements for electron/proton conduction and water/gas two-phase flow transport.[34,35] Site1 and site7 exhibited the highest Ru element content due to the poor conductivity of CL, which was consistent with conclusion drawn in other literature.[36,37] Additionally, it was observed that the Ru content initially increased and then decreased from site3 to site5, with site4 exhibiting the highest content. The touched area (site3, site4, and site5) at the PTL/CL interface was compressed due to compression force, leading to challenges for oxygen removal and water delivery. Consequently, site4 exhibited a higher Ru element content. Similar trends were observed in the aging test at 2.1 V, except for differences in the Ru element content in the touched area, which exhibited a higher Ru element content compared to in the untouched area. The difference in Ru content in the touched area for the high aging voltage was attributed to the distinct supply of reactant water. Under high aging voltage, the OER reaction rate was extremely fast and a large number of oxygen bubbles accumulated, leading to catalyst utilization in the CL being relatively uneven due to the poor water supply.[38–40]

For further quantitative analysis of the current density distribution, a numerical model was developed (see Fig. S10†), and the model information is shown in Table S1.† Fig. S11† presents the predicted porosity and electric potential distribution at the CL surface. Compared with the untouched area of the PTL/CL interface, the pores within the CL in the touched area shrank or even closed entirely due to the compression force from the titanium fibers, making it challenging for water/gas to effectively be transported, as shown in Fig. S11(a).† Besides, due to the significantly lower electrical conductivity of the CL compared to the PTL, the potential dropped rapidly near the titanium fibers, with minimal electric potential in the untouched area, as shown in Fig. S11(b).† To comprehensively analyze the influence of porosity and conductivity, we introduce the concept of a reaction rate index (RRI, where RRI = current density × mass concentration of water) to reveal the reaction rate on the CL surface. Hence, the RRI along the horizontal direction (at a specific depth in the CL domain) was quite different, with the highest values observed in the border area, followed by the touched area, and the lowest values found in the untouched area, as shown in Fig. 4(b). Next, the influence of the porosity and electric conductivity of the CL on the RRI were further studied, and the simulation results are shown in Fig. 4(c and d). The simulation results indicated that, given the considerably lower conductivity of the CL compared to the PTL, variations in the conductivity of the CL had a

Open Access Article. Published on 13 February 2024. Downloaded on 12/5/2025 3:20:50 AM.
This article is licensed under a Creative Commons Attribution-NonCommercial 3.0 Unported Licence.

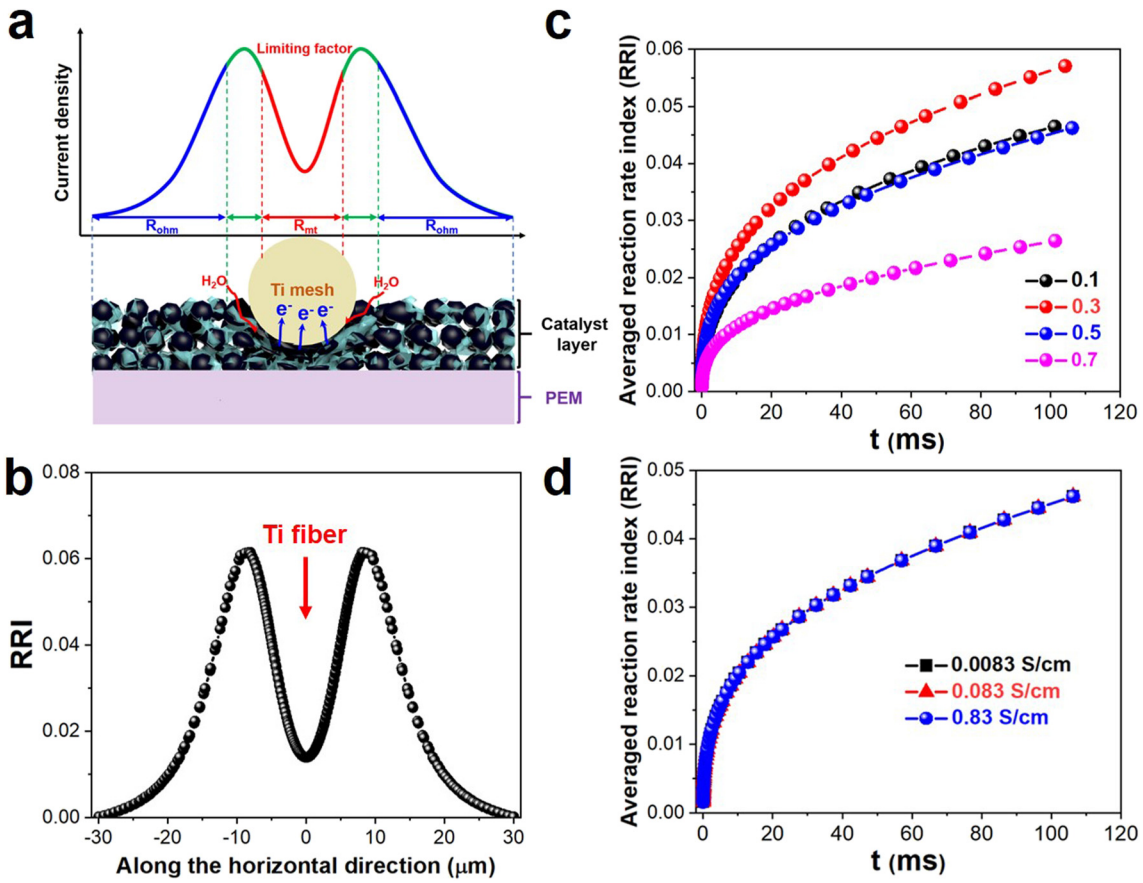

Fig. 4 (a) Schematic illustrating the distribution of current density at the micrometer scale at the interface of the PTL/CL. (b) RRI along the horizontal direction (at a specific depth in the CL domain). (c) Average reaction rate index in the ACL domain with different conductivities. (d) Average reaction rate index in the ACL domain with different porosities.

negligible effect on the distribution of the electric field, leading to a nearly constant RRI value.[36,37] While the porosity had great impact on the RRI, the value of the RRI increased and then decreased for porosities ranging from 0.1 to 0.7, with the highest value attained at 0.3, which resulted from the competition between mass transfer and the active catalyst sites. Simultaneously, the RRI value experienced a rapid increase within the initial few milliseconds, followed by a stabilization of the growth rate over the subsequent tens of milliseconds. This phenomenon arose from the significantly faster electron transport compared to mass transport (by five to six orders of magnitude).

Drawing from the experimental and simulation data, a schematic representation of the current density distribution at the PTL/CL interface is presented in Fig. 4(a). Since the voltage of the catalyst layer (U) remained constant in the chronoamperometry tests, the current density was determined by the impedance R, including R_{ct} and R_{limit}. Among these, R_{ct} remained constant while R_{limit} was composed of R_{ohm} and R_{mt}, as shown in eqn (1).

$$i = \frac{U}{R_{ct} + R_{limit}} \tag{1}$$

where, i is the current density of the catalyst layer, $R_{constant}$ is the constant impedance, and R_{limit} is the limiting impedance that affects the electrochemical performance.

At the border area of the PTL/CL interface, the electric charge conduction and water/gas two-phase flow transport occur more easily, resulting in the lowest impedance and highest current density distribution. However, for the untouched area between the PTL and CL, due to the poor in-plane conduction of the CL compared to the PTL, the catalyst cannot be efficiently utilized. Besides, mechanically induced stress and strain by the PTL and continuous creep under hydrated environments results in micro-crack formation, which hinder utilization of the catalyst in the untouched area.[35] Therefore, the current density distribution was lowest due to the higher R_{ohm}. The touched area of the current density distribution thus varies depending on the operating conditions, such as the applied cell voltage and assembly compression force, as so requires simultaneous consideration of the water/gas transport and electron conduction, representing the interplay between R_{ohm} and R_{mt}.

In summary, a straightforward and *ex situ* visible method to identify the current density distribution at the micrometer scale in the CL surface by utilizing the poor stability of RuO_2 was proposed, and a numerical model was also developed,

Open Access Article. Published on 13 February 2024. Downloaded on 12/5/2025 3:20:50 AM.
This article is licensed under a Creative Commons Attribution-NonCommercial 3.0 Unported Licence.

which was validated by the test results. The experimental and numerical results revealed that the distribution of the current density of the CL surface was uneven, indicating that the catalyst was not fully utilized. The border area of the PTL/CL interface exhibited the highest current density under any working conditions, due to meeting the requirements for electron/proton conduction and mass transport. The untouched area exhibited the lowest current density due to the poor conductivity of the CL. The untouched area exhibited varying current density under different operating conditions, which could be attributed to the combined effects of conductivity and mass transfer, such as the applied cell voltage and assembly compression force. Therefore, identifying the current density distribution at the micrometer scale provides valuable guidance for reducing precious metal loading, and designing PTL/CL interfaces more efficiently.

Conflicts of interest

There are no conflicts to declare.

Acknowledgements

This work is supported by National Key R&D Program of China (2023YFB4004604), Science and Technology Projects (RD2021010401) of the Innovation Laboratory for Sciences and Technologies of Energy Materials of Fujian Province (IKKEM) and the Science and Technology Project (2022L3077) of Fujian Province.

References

1 D. V. Esposito, Membraneless Electrolyzers for Low-Cost Hydrogen Production in a Renewable Energy Future, *Joule*, 2017, **1**(4), 651–658, DOI: **10.1016/j.joule.2017.07.003**.

2 N. R. B. Pivovar, Sunita Satyapal, Hydrogen at Scale (H_2@Scale): Key to a Clean, Economic, and Sustainable Energy System, *Electrochem. Soc. Interface*, 2018, **27**, 47–52, DOI: **10.1149/2.F04181if**.

3 K. Ayers, N. Danilovic, R. Ouimet, M. Carmo, B. Pivovar and M. Bornstein, Perspectives on Low-Temperature Electrolysis and Potential for Renewable Hydrogen at Scale, *Annu. Rev. Chem. Biomol. Eng.*, 2019, **10**(1), 219–239, DOI: **10.1146/annurev-chembioeng-060718-030241**.

4 C. Feng, M. Lv, J. Shao, H. Wu, W. Zhou, S. Qi, C. Deng, X. Chai, H. Yang, Q. Hu and C. He, Lattice Strain Engineering of Ni_2P Enables Efficient Catalytic Hydrazine Oxidation-Assisted Hydrogen Production, *Adv. Mater.*, 2023, **35**(42), 2305598, DOI: **10.1002/adma.202305598**.

5 X. Li, H. Zhang, Q. Hu, W. Zhou, J. Shao, X. Jiang, C. Feng, H. Yang and C. He, Amorphous NiFe Oxide-based Nanoreactors for Efficient Electrocatalytic Water Oxidation, *Angew. Chem., Int. Ed.*, 2023, **62**(15), e202300478, DOI: **10.1002/anie.202300478**.

6 M. Carmo, D. L. Fritz, J. Mergel and D. Stolten, A comprehensive review on PEM water electrolysis, *Int. J. Hydrogen Energy*, 2013, **38**(12), 4901–4934, DOI: **10.1016/j.ijhydene.2013.01.151**.

7 O. Schmidt, A. Gambhir, I. Staffell, A. Hawkes, J. Nelson and S. Few, Future cost and performance of water electrolysis: An expert elicitation study, *Int. J. Hydrogen Energy*, 2017, **42**(52), 30470–30492, **https://creativecommons.org/licenses/by/4.0/**.

8 A. Buttler and H. Spliethoff, Current status of water electrolysis for energy storage, grid balancing and sector coupling via power-to-gas and power-to-liquids: A review, *Renewable Sustainable Energy Rev.*, 2018, **82**, 2440–2454, DOI: **10.1016/j.rser.2017.09.003**.

9 F. Hegge, F. Lombeck, E. Cruz Ortiz, L. Bohn, M. von Holst, M. Kroschel, J. Hübner, M. Breitwieser, P. Strasser and S. Vierrath, Efficient and Stable Low Iridium Loaded Anodes for PEM Water Electrolysis Made Possible by Nanofiber Interlayers, *ACS Appl. Energy Mater.*, 2020, **3**(9), 8276–8284, DOI: **10.1021/acsaem.0c00735**.

10 W. Wang, S. Yu, K. Li, L. Ding, Z. Xie, Y. Li, G. Yang, D. A. Cullen, H. Yu, Z. Kang, J. A. Wrubel, Z. Ma, G. Bender, C. B. Capuano, A. Keane and F.-Y. Zhang, Insights into the rapid two-phase transport dynamics in different structured porous transport layers of water electrolyzers through high-speed visualization, *J. Power Sources*, 2021, **516**(31), 230641, DOI: **10.1016/j.jpowsour.2021.230641**.

11 J. Kwen, G. Doo, S. Choi, H. Guim, S. Yuk, D.-H. Lee, D. W. Lee, J. Hyun and H.-T. Kim, Identification of the electrical connection in the catalyst layer of the polymer electrolyte membrane water electrolyzer, *Int. J. Hydrogen Energy*, 2022, **47**(30), 14017–14026, DOI: **10.1016/j.ijhydene.2022.02.136**.

12 C. Immerz, B. Bensmann, P. Trinke, M. Suermann and R. Hanke-Rauschenbach, Spatially Resolved Current Density Mapping in PEM-Water Electrolysis Cells, *Chem. Ing. Tech.*, 2019, **91**(6), 907–918, DOI: **10.1002/cite.201800175**.

13 F. H. Roenning, A. Roy, D. S. Aaron and M. M. Mench, Mass transport limitations in polymer electrolyte water electrolyzers using spatially-resolved current measurement, *J. Power Sources*, 2022, **542**(15), 231749, DOI: **10.1016/j.jpowsour.2022.231749**.

14 C. Y. Lee, C. H. Chen, H. C. Chuang, H. T. Hsieh and Y. C. Chiu, Long-Acting Real-Time Microscopic Monitoring Inside the Proton Exchange Membrane Water Electrolyzer, *Sensors*, 2023, **23**(12), 5595, DOI: **10.3390/s23125595**.

15 Z. Kang, S. M. Alia, M. Carmo and G. Bender, In-situ and in-operando analysis of voltage losses using sense wires for proton exchange membrane water electrolyzers, *J. Power Sources*, 2021, **481**(1), 229012, DOI: **10.1016/j.jpowsour.2020.229012**.

16 Z. Kang, H. Wang, Y. Liu, J. Mo, M. Wang, J. Li and X. Tian, Exploring and understanding the internal voltage losses through catalyst layers in proton exchange membrane water electrolysis devices, *Appl. Energy*, 2022, **317**(1), 119213, DOI: **10.1016/j.apenergy.2022.119213**.

17 Y. Li, Z. Kang, X. Deng, G. Yang, S. Yu, J. Mo, D. A. Talley, G. K. Jennings and F.-Y. Zhang, Wettability effects of thin titanium liquid/gas diffusion layers in proton exchange membrane electrolyzer cells, *Electrochim. Acta*, 2019, **298**, 704–708, DOI: **10.1016/j.electacta.2018.12.162**.

18 J. Mo, G. Yang, Y. Li, Z. Kang, G. Bender, B. S. Pivovar, J. B. Green and F.-Y. Zhang, Experimental studies on the effects of sheet resistance and wettability of catalyst layer on electro-

Open Access Article. Published on 13 February 2024. Downloaded on 12/5/2025 3:20:50 AM.
This article is licensed under a Creative Commons Attribution-NonCommercial 3.0 Unported Licence.

catalytic activities for oxygen evolution reaction in proton exchange membrane electrolysis cells, *Int. J. Hydrogen Energy*, 2020, **45**(51), 26595–26603, DOI: 10.1016/j.ijhydene.2020.07.087.

19 J. Mo, G. Yang, Y. Li, Z. Kang, G. Bender, B. S. Pivovar, J. B. Green and F.-Y. Zhang, Experimental studies on the effects of sheet resistance and wettability of catalyst layer on electro-catalytic activities for oxygen evolution reaction in proton exchange membrane electrolysis cells, *Int. J. Hydrogen Energy*, 2020, **45**(51), 26595–26603, DOI: 10.1016/j.electacta.2021.137751.

20 W. Wang, K. Li, L. Ding, S. Yu, Z. Xie, D. A. Cullen, H. Yu, G. Bender, Z. Kang, J. A. Wrubel, Z. Ma, C. B. Capuano, A. Keane, K. Ayers and F. Y. Zhang, Exploring the Impacts of Conditioning on Proton Exchange Membrane Electrolyzers by In Situ Visualization and Electrochemistry Characterization, *ACS Appl. Mater. Interfaces*, 2022, **14**(7), 9002–9012, DOI: 10.1021/acsami.1c21849.

21 S. Chen, H. Huang, P. Jiang, K. Yang, J. Diao, S. Gong, S. Liu, M. Huang, H. Wang and Q. Chen, Mn-Doped RuO_2 Nanocrystals as Highly Active Electrocatalysts for Enhanced Oxygen Evolution in Acidic Media, *ACS Catal.*, 2019, **10**(2), 1152–1160, DOI: 10.1021/acscatal.9b04922.

22 M. A. Hubert, A. M. Patel, A. Gallo, Y. Liu, E. Valle, M. Ben-Naim, J. Sanchez, D. Sokaras, R. Sinclair, J. K. Nørskov, L. A. King, M. Bajdich and T. F. Jaramillo, Acidic Oxygen Evolution Reaction Activity-–Stability Relationships in Ru-Based Pyrochlores, *ACS Catal.*, 2020, **10**(20), 12182–12196, DOI: 10.1021/acscatal.0c02252.

23 H. Huang, H. Kim, A. Lee, S. Kim, W.-G. Lim, C.-Y. Park, S. Kim, S.-K. Kim and J. Lee, Structure engineering defective and mass transfer-enhanced RuO_2 nanosheets for proton exchange membrane water electrolyzer, *Nano Energy*, 2021, **88**, 106276, DOI: 10.1016/j.nanoen.2021.106276.

24 J. He, W. Li, P. Xu and J. Sun, Tuning electron correlations of RuO_2 by co-doping of Mo and Ce for boosting electrocatalytic water oxidation in acidic media, *Appl. Catal., B*, 2021, **298**(5), 120528, DOI: 10.1016/j.apcatb.2021.120528.

25 Q. Hu, K. Gao, X. Wang, H. Zheng, J. Cao, L. Mi, Q. Huo, H. Yang, J. Liu and C. He, Subnanometric Ru clusters with upshifted D band center improve performance for alkaline hydrogen evolution reaction, *Nat. Commun.*, 2022, **13**(1), 3958, DOI: 10.1038/s41467-022-31660-2.

26 X. Li, C. Deng, Y. Kong, Q. Huo, L. Mi, J. Sun, J. Cao, J. Shao, X. Chen, W. Zhou, M. Lv, X. Chai, H. Yang, Q. Hu and C. He, Unlocking the Transition of Electrochemical Water Oxidation Mechanism Induced by Heteroatom Doping, *Angew. Chem., Int. Ed.*, 2023, **62**(40), e202309732, DOI: 10.1002/anie.202309732.

27 R. Kötz, S. Stucki, D. Scherson and D. M. Kolb, In-situ identification of RuO_4 as the corrosion product during oxygen evolution on ruthenium in acid media, *J. Electroanal. Chem. Interfacial Electrochem.*, 1984, **172**, 211–219, DOI: 10.1016/0022-0728(84)80187-4.

28 M. Santos, D. Miwa and S. Machado, Study of anion adsorption on polycrystalline Pt by electrochemical quartz crystal microbalance, *Electrochem. Commun.*, 2000, **2**(10), 692–696, DOI: 10.1016/S1388-2481(00)00102-8.

29 G. Doo, J. Park, J. Park, J. Heo, J. Jung, D. W. Lee, H. Bae, J. Hyun, E. Oh, J. Kwen, K. M. Kim and H.-T. Kim, Contact Problems of IrO_x Anodes in Polymer Electrolyte Membrane Water Electrolysis, *ACS Energy Lett.*, 2023, **8**(5), 2214–2220, DOI: 10.1021/acsenergylett.3c00291.

30 T. Morawietz, M. Handl, C. Oldani, K. A. Friedrich and R. Hiesgen, Influence of Water and Temperature on Ionomer in Catalytic Layers and Membranes of Fuel Cells and Electrolyzers Evaluated by AFM, *Fuel Cells*, 2018, **18**(3), 239–250, DOI: 10.1002/fuce.201700113.

31 T. Morawietz, M. Handl, C. Oldani, P. Gazdzicki, J. Hunger, F. Wilhelm, J. Blake, K. A. Friedrich and R. Hiesgen, High-Resolution Analysis of Ionomer Loss in Catalytic Layers after Operation, *J. Electrochem. Soc.*, 2018, **165**(6), F3139–F3147, DOI: 10.1149/2.0151806jes.

32 A. Zagalskaya and V. Alexandrov, Role of Defects in the Interplay between Adsorbate Evolving and Lattice Oxygen Mechanisms of the Oxygen Evolution Reaction in RuO_2 and IrO_2, *ACS Catal.*, 2020, **10**(6), 3650–3657, DOI: 10.1021/acscatal.9b05544.

33 S. Hao, H. Sheng, M. Liu, J. Huang, G. Zheng, F. Zhang, X. Liu, Z. Su, J. Hu, Y. Qian, L. Zhou, Y. He, B. Song, L. Lei, X. Zhang and S. Jin, Torsion strained iridium oxide for efficient acidic water oxidation in proton exchange membrane electrolyzers, *Nat. Nanotechnol.*, 2021, **16**(12), 1371–1377, DOI: 10.1038/s41565-021-00986-1.

34 Y. Li, Z. Kang, J. Mo, G. Yang, S. Yu, D. A. Talley, B. Han and F.-Y. Zhang, In-situ investigation of bubble dynamics and two-phase flow in proton exchange membrane electrolyzer cells, *Int. J. Hydrogen Energy*, 2018, **43**(24), 11223–11233, DOI: 10.1016/j.ijhydene.2018.05.006.

35 J. Lopata, Z. Kang, J. Young, G. Bender, J. W. Weidner and S. Shimpalee, Effects of the Transport/Catalyst Layer Interface and Catalyst Loading on Mass and Charge Transport Phenomena in Polymer Electrolyte Membrane Water Electrolysis Devices, *J. Electrochem. Soc.*, 2020, **167**(6), 064507, DOI: 10.1149/ 1945-7111/ab7f87.

36 J. Mo, Z. Kang, S. T. Retterer, D. A. Cullen, T. J. Toops, J. B. Green, M. M. Mench and F.-Y. Zhang, Discovery of true electrochemical reactions for ultrahigh catalyst mass activity in water splitting, *Sci. Adv.*, 2016, **2**, e1600690, DOI: 10.1126/sciadv.1600690.

37 J. Mo, Z. Kang, G. Yang, Y. Li, S. T. Retterer, D. A. Cullen, T. J. Toops, G. Bender, B. S. Pivovar, J. B. Green Jr and F.-Y. Zhang, In situ investigation on ultrafast oxygen evolution reactions of water splitting in proton exchange membrane electrolyzer cells, *J. Mater. Chem. A*, 2017, **5**(35), 18469–18475, DOI: 10.1039/c7ta05681h.

38 T. Schuler, R. De Bruycker, T. J. Schmidt and F. N. Büchi, Polymer Electrolyte Water Electrolysis: Correlating Porous Transport Layer Structural Properties and Performance: Part I. Tomographic Analysis of Morphology and Topology, *J. Electrochem. Soc.*, 2019, **166**(4), F270–F281, DOI: 10.1149/2.0561904jes.

39 T. Schuler, T. J. Schmidt and F. N. Büchi, Polymer Electrolyte Water Electrolysis: Correlating Performance and Porous Transport Layer Structure: Part II. Electrochemical Performance

 This journal is © The Royal Society of Chemistry 2024

Open Access Article. Published on 13 February 2024. Downloaded on 12/5/2025 3:20:50 AM.
This article is licensed under a Creative Commons Attribution-NonCommercial 3.0 Unported Licence.

Analysis, *J. Electrochem. Soc.*, 2019, **166**(10), F555–F565, DOI: 10.1149/2.1241908jes.

40 X. Peng, P. Satjaritanun, Z. Taie, L. Wiles, A. Keane, C. Capuano, I. V. Zenyuk and N. Danilovic, Insights into Interfacial and Bulk Transport Phenomena Affecting Proton Exchange Membrane Water Electrolyzer Performance at Ultra-Low Iridium Loadings, *Adv. Sci.*, 2021, **8**(21), 2102950, DOI: 10.1002/advs.202102950.